Climate change threatens terrestrial water storage over the Tibetan Plateau

Xueying Li [1], Di Long [1 ✉], Bridget R. Scanlon [2], Michael E. Mann [3], Xingdong Li [1], Fuqiang Tian [1], Zhangli Sun[1] and Guangqian Wang[1]

Terrestrial water storage (TWS) over the Tibetan Plateau, a major global water tower, is crucial in determining water transport and availability to a large downstream sian population. Climate change impacts on historical and future TWS changes, however, are not well quantified. Here we used bottom-up and top-down approaches to quantify a significant TWS decrease (10.2 Gt yr^{-1}) over the Tibetan Plateau in recent decades (2002–2017), reflecting competing effects of glacier retreat, lake expansion and sub-surface water loss. Despite the weakened trends in projected TWS, it shows large declines under a mid-range carbon emissions scenario by the mid-twenty-first century. Excess water-loss projections for the mu Darya and Indus basins present a critical water resource threat, indicating declines of 119% and 79% in water-supply capacity, respectively. Our study highlights these two hotspots as being at risk from climate change, informing adaptation strategies for these highly vulnerable regions.

Known as the water towers of Asia, the Tibetan Plateau (TP) supplies a substantial portion of the water demand for almost 2 billion people[1]. Unique high-elevation terrain and atmospheric circulation dominated by monsoons and upper-level westerly winds[2,3] jointly generate precious freshwater resources in this region. Relatively undisturbed by human activities, the TP has an average elevation exceeding 4 km and serves as an important regulator of the Asian monsoon system. Terrestrial water storage (TWS), including all forms of surface and subsurface components, is crucial in determining hydrologic transport and water availability[4] but is highly sensitive to climate change[5]. Furthermore, water storage is impacted by climate extremes, such as droughts[6,7] and floods[8,9], and is linked to global sea-level rise[10,11]. TWS change is thus a critical indicator of vulnerability of global water towers[12]. Despite its importance, the impact of climate change on historical and future TWS over the TP remains largely underexplored in past work, due primarily to uncertainties in observations and models in the presence of extremely complex terrain and atmospheric circulation. Challenges in interpreting satellite-based TWS observations at large scales and in explicitly resolving all TWS components in hydrologic modelling[13,14] hinder precise assessments of the historical response of TWS to observed climate change. Moreover, there are no existing studies of the potential response of TWS over the TP to projected future climate change. Although a study by Pokhrel et al.[15] linked projected future drought changes to TWS at the global scale, it did not assess changes over much of the TP (Supplementary Fig. 1), where potential changes in TWS threaten large downstream Asian populations.

Long-term TWS changes across the TP result mainly from changes in glacier mass balance, lake volumes and subsurface water storage, although TWS is also influenced by other components that vary mostly at seasonal to interannual timescales (for example, snow, canopy and reservoir water storage). Because of an increasingly warm and wet climate, water storage over the TP has changed substantially during the past two decades. Contributing factors include glacier retreat over the southeastern TP[16,17], glacial

mass gain in the Karakoram Mountains (Karakoram anomaly)[18,19], lake expansion over the Inner TP[20,21] and widespread permafrost degradation[22,23].

Most past studies have been limited to a subset of TWS components (for example, glacier mass or lake water storage) quantified using one specific method (for example, observational analysis, modelling or diagnosis via remote sensing). Such studies have not yielded a comprehensive assessment of contributions to TWS changes. Advances in Gravity Recovery and Climate Experiment (GRACE) and GRACE Follow-On (GRACE-FO) satellite missions have yielded mature products over the past two decades[4,24,25], providing an unprecedented opportunity to quantify TWS changes at large scales. However, GRACE products are poorly constrained over the TP, displaying extreme sensitivity to underlying assumptions of analytical methods used (for example, spherical harmonic versus mascon solutions)[26]. There is consequently no consensus on TWS changes in this region. Previous studies have not explored the sensitivity of GRACE solutions using independent data sources. A reliable benchmark for the magnitude of TWS changes over the TP has thus been lacking. The absence of future projections of TWS, moreover, limits any guidance on policymaking, despite the fact that the TP has long been considered a climate change hotspot[12,27].

In this Article, we attempt to fill these knowledge gaps by exploring climate impacts on historical and future projected TWS changes over the TP, which includes seven exorheic (open) and five endorheic (closed) basins[28] (Fig. 1 and Supplementary Table 1). Using top-down (based on GRACE) and bottom-up (based on component storages) approaches combined with machine-learning techniques, we integrated multisource remote sensing, land surface models (LSMs) and global climate model results (Supplementary Tables 2 and 3) to provide a benchmark of observed TWS changes over the past two decades (2002–2020) and projections over the next four decades (2021–2060). Climatic mechanisms (precipitation, air temperature and surface short-wave radiation) underlying the historical and future TWS changes were

[1]State Key Laboratory of Hydroscience and Engineering, Department of Hydraulic Engineering, Tsinghua University, Beijing, China. [2]Bureau of Economic Geology, Jackson School of Geosciences, The University of Texas at ustin, ustin, TX, US . [3]Department of Meteorology and tmospheric Science, Penn State University, University Park, P , US . ✉e-mail: dlong@tsinghua.edu.cn
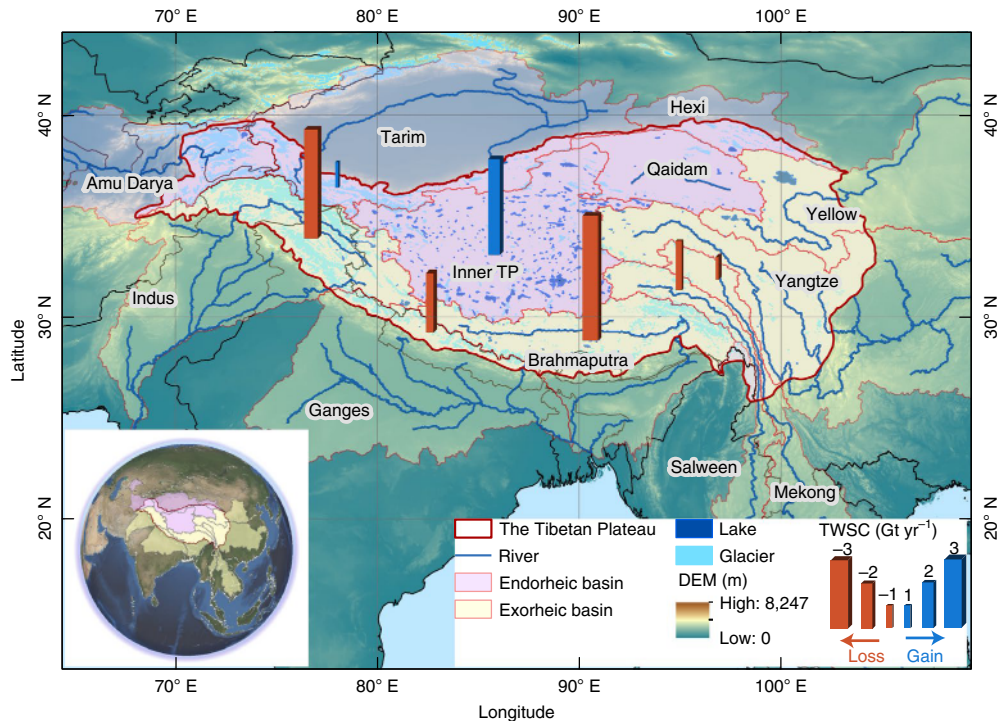
Fig. 1 | Lakes, glaciers and major river basins on the TP. Endorheic basins are shown in light purple and exorheic basins in light yellow. Bar plots show TWSC for each basin (only basins with TWS trends ≥ 1.0 Gt yr⁻¹ are shown) during 2002–2017, estimated from the GR CE JPL-M solution. Blue bars represent mass gain; red bars represent mass loss. Bar sizes represent the magnitude of TWSC (Gt yr⁻¹). DEM, digital elevation model.

examined to better understand the response of TWS to a changing climate. Moreover, we assessed the vulnerability of water-supply security caused by storage changes by the mid-twenty-first century (up to 2060) in a preliminary attempt to reveal potential threats to water security in key Asian basins (Methods and Supplementary Fig. 2). Recognizing that projected climate trends over the TP show slight differences among different forcing scenarios under the shared socioeconomic pathways (for example, SSP1–2.6, SSP2–4.5 and SSP5–8.5) by the mid-twenty-first century (Extended Data Fig. 1), we selected the mid-range forcing scenario, SSP2–4.5, from the Coupled Model Intercomparison Project phase 6 (CMIP6) database for the purpose of detailed projections.

TWSC over the past two decades

During the GRACE observation period (April 2002–June 2017), four solutions of top-down GRACE observations (CSR-M (Center for Space Research-mascon), JPL-M (Jet Propulsion Laboratory-mascon), CSR-SH (spherical harmonics) and JPL-SH) generally show significant decreases in TWS in the exorheic basins and increases in the endorheic basins (Extended Data Fig. 2). However, there are large discrepancies in the magnitude of the TWS changes (TWSC) from different GRACE solutions, particularly in the endorheic Tarim and Inner TP basins (Extended Data Fig. 3). In general, TWSC for the two SH solutions are similar but differ markedly from the two mascon solutions. We summed storage changes in glaciers, lakes and subsurface components to estimate bottom-up TWSC (Supplementary Table 4) and found good agreement between TWS trends derived from the top-down JPL-M analysis and those derived from the bottom-up approach in most of the study regions (9 out of 10) (Fig. 2 and Supplementary Table 5). Using bottom-up TWSC as a reference, an important advantage of JPL-M is that it successfully detects significant increases in TWS over the endorheic region (particularly in the Inner TP), where SH and mascon solutions show opposite trends relative to each

other. In most cases, JPL-M displays the greatest magnitudes for both decreasing and increasing trends (Supplementary Table 5). However, the consistency between TWSC from JPL-M and from the bottom-up approach here indicates that JPL-M probably provides reliable estimates for regions that are vulnerable to diminished water resources, contrasting with previous studies suggesting it overestimates TWSC[26].

TWS over the entire TP decreased by 10.2 Gt yr⁻¹ (P 0.05) during the GRACE period (2002–2017) on the basis of JPL-M, reflecting the balance between a decreasing trend in the exorheic region (−15.8 Gt yr⁻¹; P 0.05) and an increasing trend in the endorheic region (5.6 Gt yr⁻¹; P 0.05). Significant TWS declines were attributed mainly to glacier retreat over the Hindu Kush–Himalayan–Nyainqentanglha mountains (for example, −10.1 Gt yr⁻¹ across the Indus–Ganges–Brahmaputra region), and the subsurface depletion that may be associated with degradation of seasonally frozen ground[23] (for example, −1.8 Gt yr⁻¹ across the Salween–Mekong basins). However, large increases in TWS were caused by lake expansion (for example, 5.8 Gt yr⁻¹ in the Inner TP basin) and glacier mass gain across the Karakoram and Western Kun Lun Mountains (for example, 0.9 Gt yr⁻¹ in the Tarim basin) (Supplementary Table 6). Water-storage changes over the TP are highly linked to downstream water availability (for example, melt water for irrigation[29,30]) and natural disasters (for example, glacier collapse[31] and lake outburst[32,33]). Patterns of TWSC in individual basins and associated threats are comprehensively discussed in Supplementary Section 1.

Future TWSC under climate change

Under a mid-range forcing scenario (SSP2–4.5), the magnitude of projected TWS trends in most TP basins is greatly reduced by the mid-twenty-first century, while the Amu Darya and Indus basins may continue to experience ongoing significant TWS losses (Fig. 3a–c and Extended Data Fig. 4). In the coming decade (2021–2030), the Amu Darya basin may emerge as a hotspot of
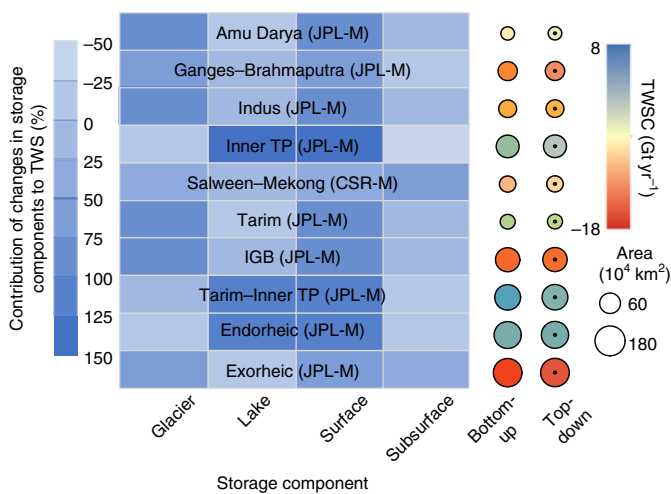
Fig. 2 | Component contributions and agreement in water-storage changes. The study region and the GRACE solution that agrees best with the bottom-up derived TWSC in each region are presented in each row. Four box columns on the left indicate contributions of different storage components (including glacier, lake, surface and subsurface water storages; shown at the bottom) to TWSC by different colour saturations. Two circle columns on the right show rates of TWSC, where circles without a centre mark represent those derived from the bottom-up approach and circles with a centre mark represent those derived from the top-down approach. Circle size indicates area of each study region.

water-storage depletion with the magnitude of TWS decrease $(1.2 \pm 0.5\,\mathrm{Gt\,yr^{-1}}; P < 0.05)$ about twice as large as that during the GRACE period $(2002\text{--}2017; 0.7\,\mathrm{Gt\,yr^{-1}})$. The projected TWS trend for the Indus basin $(-5.7 \pm 0.7\,\mathrm{Gt\,yr^{-1}}; P < 0.05)$ is similar in magnitude to that during the GRACE period $(-4.8\,\mathrm{Gt\,yr^{-1}})$, whereas the spatial extent of TWS declines becomes larger (Fig. 3b). In contrast to the Amu Darya and Indus basins, other regions over the TP show reduced trends or unchanging TWS in the coming decade. By the mid-twenty-first century, most areas over the TP show little trend in TWS with the exception of slight TWS declines in the Indus basin. The large decrease in projected TWS over the Amu Darya basin during the coming decade (2021–2030), in particular, does not extend to the mid-twenty-first century (Fig. 3c). This indicates that TWS approaches a new equilibrium after decades of glacier retreat, lake expansion and frozen soil degradation. This conclusion is supported by separate projections of glacier mass balance[34], indicating that glacier melt in major river basins on the TP (for example, Brahmaputra and Ganges) peaks over the next two decades followed by a decrease.

Although TWS trends are weakened, we found large climate change impacts on TWS over the TP by the mid-twenty-first century (Fig. 3d). TWS is projected to decline substantially from the early (2002–2030) to mid (2031–2060) twenty-first century in the Amu Darya and Indus basins with losses of ~23 Gt (equivalent to 18 cm for basin-averaged water depth) and ~105 Gt (33 cm), respectively. In addition, the Ganges–Brahmaputra and Salween–Mekong basins show mass losses of ~66 Gt (14 cm) and ~26 Gt (13 cm) by the mid (2031–2060) twenty-first century relative to the 2002–2030 period. Slight mass gain of ~6 Gt is projected in the endorheic Tarim–Inner TP–Qaidam basins. However, the magnitude of this mass gain is likely to be compensated by the large TWS decline over the entire TP, with a net mass loss of ~230 Gt by the mid-twenty-first century. Compared with TWSC in the past two decades, the greatest threats to future water resources are found in the glacier-dominated Amu Darya and Indus basins. Subsurface-dominated TWSC

(the Salween–Mekong region) and lake-dominated TWSC (the Inner TP basin), by contrast, are projected to be relatively stable.

The combined effects of climate drivers, including precipitation, temperature and surface short-wave radiation, generally explain projected TWS variations in the future. Most areas over the TP show stable annual precipitation between the early (2002–2030) and mid (2031–2060) twenty-first century. Important exceptions are the Ganges–Brahmaputra and Salween–Mekong regions, both of which show increases (Fig. 3e). Precipitation in the Ganges–Brahmaputra basin shifts from displaying a decreasing trend in the early twenty-first century (Box 1; Extended Data Fig. 5) to an increasing trend by the mid-twenty-first century (Fig. 3e). Increases in precipitation tend to dampen TWS declines in the Ganges–Brahmaputra and Salween–Mekong regions. The entire TP is projected to see a warming trend without obvious hotspots (Fig. 3f). However, both the Amu Darya and Indus basins may be more sensitive to projected warming because they have experienced stable or slightly decreasing trends in temperature over the historical period (Box 1; Extended Data Fig. 5). These findings are generally consistent with glacier projections by Rounce et al.[34] showing that glaciers over the Eastern Himalayas (the Brahmaputra basin) are likely to experience less mass loss than those in other TP regions, while the Pamir–Alay (the Amu Darya basin) is projected to see greater mass loss in the future. Surface short-wave radiation mainly impacts changes in glacier mass balance in the Tarim basin (Box 1), and stable short-wave radiation by the mid-twenty-first century could explain the slight TWSC in this case (Fig. 3g).

Potential threats of future water supply

The TP is an important source region of freshwater for downstream areas, and water storage over the TP provides a buffering capacity for water resources by supplying glacier melt water during hot and/or dry years. However, climate change could deplete TWS and weaken upstream water-supply capacity, which may threaten downstream water availability. In this Article, we quantified the vulnerability of water supply for downstream basins caused by upstream storage changes under the mid-range forcing scenario. The Amu Darya basin and seven exorheic basins (Indus, Ganges–Brahmaputra, Salween–Mekong, Yangtze and Yellow) were selected for this analysis because of large populations and water demand in the downstream areas. Irrigation, industrial, and domestic water demands were summed to total water demand (D) for downstream areas. Two sources of water supply, natural supply capacity (NSC, defined as precipitation minus actual evapotranspiration (ET)) and storage supply capacity (SSC, defined as TWS over the upstream areas) were considered (Methods). We found that in the Ganges–Brahmaputra, Salween–Mekong and Yangtze basins, total water demand in the downstream areas can be met by downstream NSC ($\mathrm{NSC_d}$) (Supplementary Table 7). This means that in these basins, changes in SSC from upstream water towers may not seriously threaten downstream water availability.

However, the Amu Darya and Indus basins could be highly dependent on upstream SSC because water demand in populated downstream areas cannot be met by $\mathrm{NSC_d}$ (Supplementary Table 7). This is generally consistent with previous studies on the impact of warming-induced changes in melt water in the region; that is, the Indus is more vulnerable to glacier loss than is the Ganges–Brahmaputra[29], and the Amu Darya is highly dependent on snow melt[35]. Over these two basins, future water demand during the mid-twenty-first century (2031–2060) remains generally stable relative to demand during the early twenty-first century (2002–2030), attributed to the slight decrease in irrigation water use but the increase in industrial and domestic water demand (Supplementary Fig. 3). Future natural supply (NSC in upstream and downstream areas) is also relatively stable during the 30 yr averaged period, although interannual variability exists.
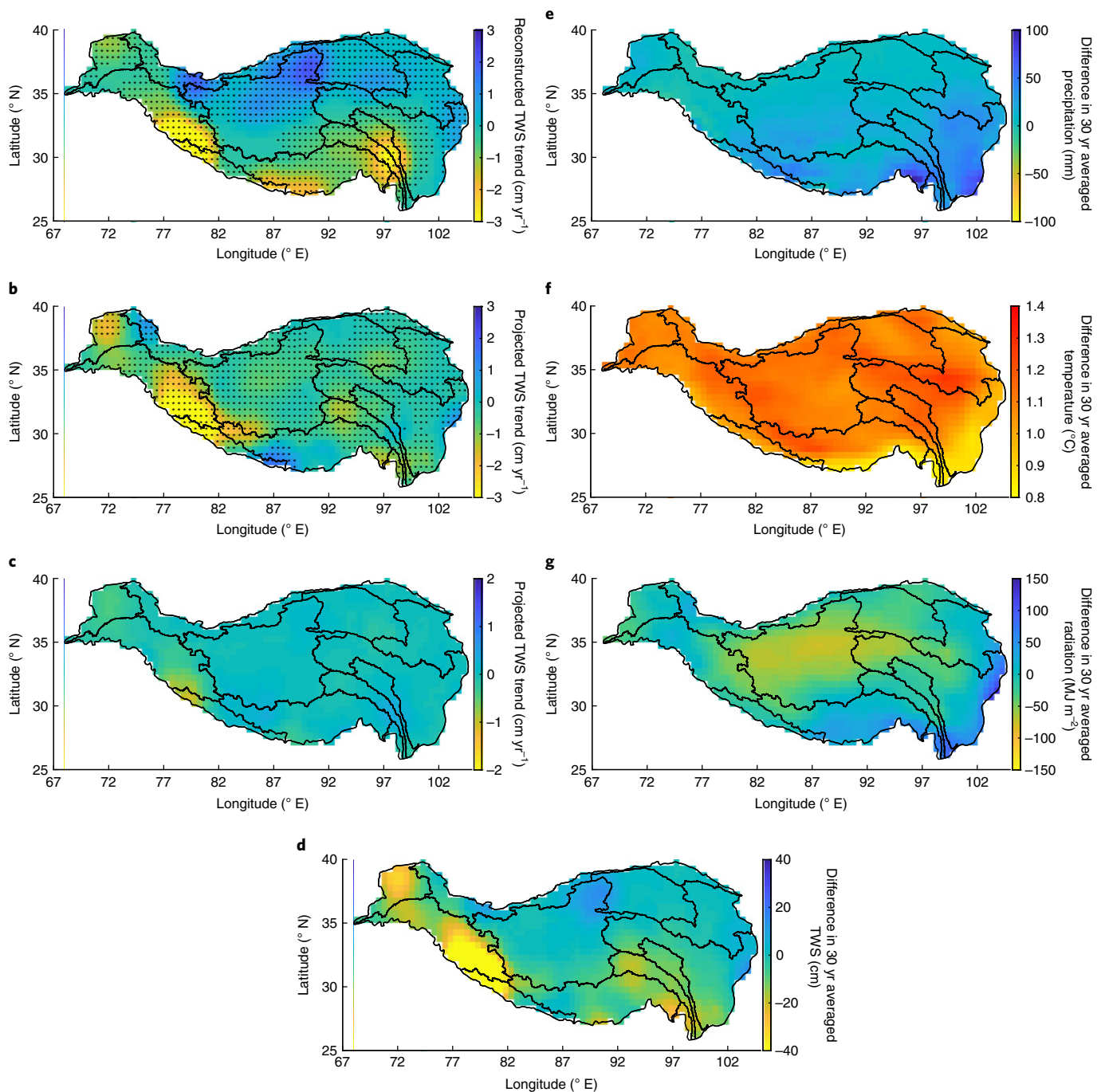
Fig. 3 | Reconstructed and projected changes in water storage and climate drivers. a–c, Spatial patterns of linear trends in machine-learning reconstructed and projected TWS on the Tibetan Plateau during the past two decades (2002–2020) (**a**), the coming decade (2021–2030) (**b**) and the mid-twenty-first century (2031–2060) (**c**). Stippling in **a** and **b** marks regions that have a significant trend (the Mann–Kendall test at a 5% significance level). **d–g**, The difference between the 30 yr averaged state for the 2031–2060 period relative to the average for the 2002–2030 period in projected TWS (**d**), annual precipitation (**e**), annual average temperature (**f**) and annual surface short-wave radiation (**g**). ll results were estimated from the ensemble mean of nine CMIP6 models under the mid-range SSP2–4.5 scenario.

In contrast to the stable water demand and NSC, the large decline in SSC could represent a major threat in the future. Taking total water demand during the early twenty-first century (2002–2030) as the baseline, projected SSC declines are up to 119% (Amu Darya) and 79% (Indus) of the demand baseline until the mid-twenty-first century (2031–2060) (Fig. 4). In particular, if assuming the same contribution of changes in surface water storage to TWSC between the future and GRACE period, the decline in surface SSC (SSCs) could account for 105% and 72% of the demand baseline, respectively.

Given that surface water directly contributes to glacier melt water, such large declines in SSCs should amplify future water shortages in these two hotspots. More alternative water-supply sources, including increased groundwater extraction and more water transfer projects, may be required to meet future water demand. Given the existing large groundwater depletion[36], rapidly growing population[37] and considerable hydro-political tension[38] along the Amu Darya and Indus rivers, our findings highlight the potential for largely amplified water crises and the importance of protecting these two water towers.

Box 1 | Impacts of climate drivers on TWSC

Climate mechanisms underlying historical TWSC during 2002–2017 are related to changes in monsoon-dominated precipitation and warming-induced precipitation phase and different roles in temperature rising and surface short-wave radiation across the TP (see Supplementary Section 2 for more details). Significant TWS declines over the Ganges–Brahmaputra basins may be jointly explained by decreases in precipitation due to the recent weakening of the South Asia Summer Monsoon and rising temperatures, especially in winter. For the Indus basin, although it is less affected by the South Asia monsoon and annual precipitation shows little change, we find decreases in winter precipitation. Salween–Mekong has undergone a warming trend that may largely drive TWS declines, resulting in not only the negative glacier mass balance, but also depletion in subsurface water storage related to degradation of seasonally frozen ground.

Despite a warming trend over the Tarim basin, the decreasing trend in surface short-wave radiation, particularly across the Karakoram and Western Kun Lun mountains, is more important in driving glacier mass gain over this region. In the Inner TP, annual precipitation features an increasing trend in the north but a decreasing trend in the south, which shows a consistent spatial pattern with TWSC. Both annual precipitation and average temperature remain almost stable in the Amu Darya basin, protecting glaciers here from rapid retreat relative to what happened over the Indus–Ganges–Brahmaputra region. Moreover, we find a warming-induced change in precipitation phase from snowfall to rainfall over the Indus, Ganges–Brahmaputra and Amu Darya basins, which could be related to large glacier retreat during past decades.
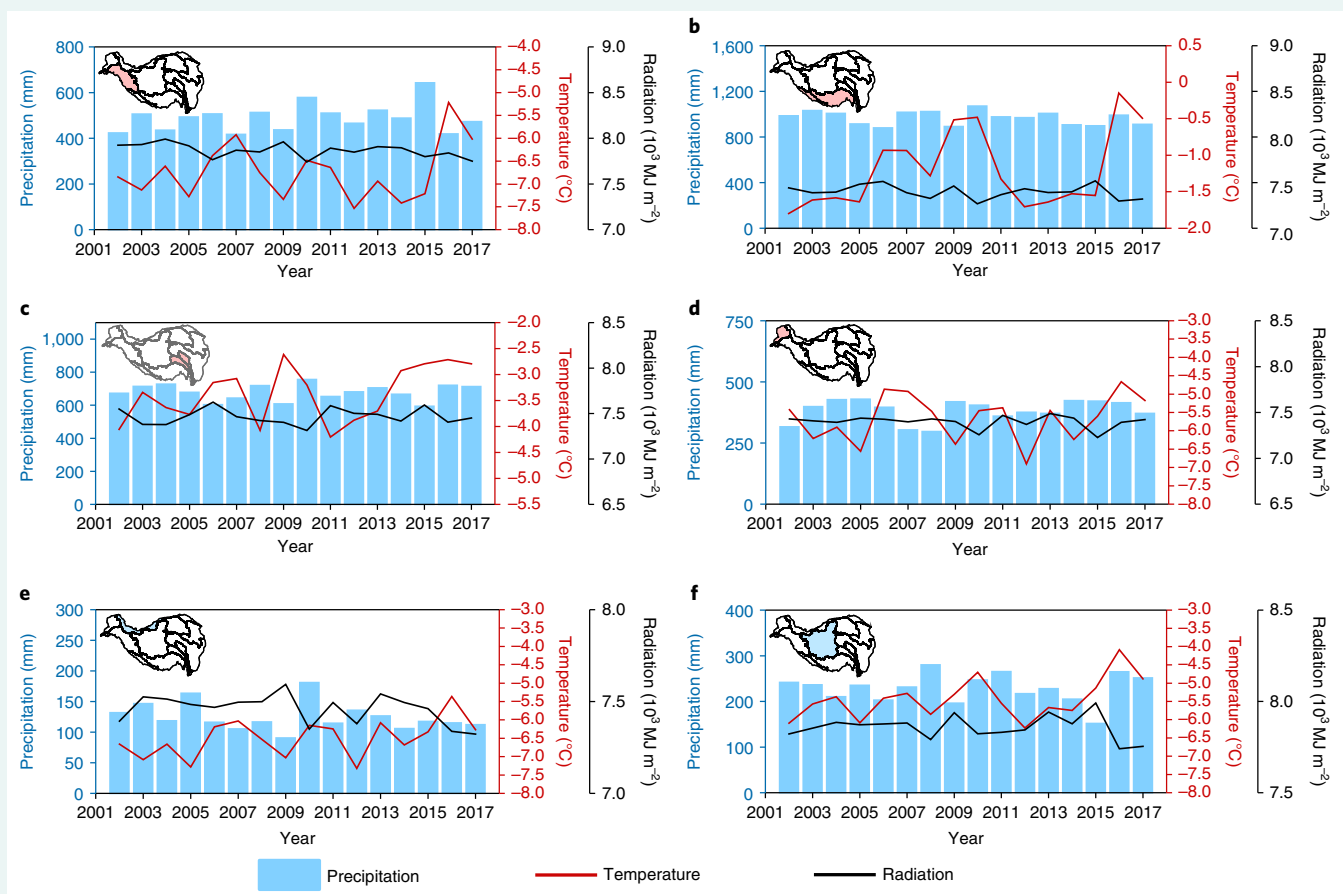
nnual variations in climate drivers of key basins during 2002–2017. **a**–**f**, nnual precipitation (light blue bars) is shown on the left *y* axis; annual average 2 m temperature (red lines) and annual surface short-wave radiation (black lines) are shown on the right *y* axis. Shadow region of the inserted Tibetan Plateau boundary on the top-left corner denotes geographical location of each river basin: Indus (**a**), Ganges–Brahmaputra (**b**), Salween–Mekong (**c**), mu Darya (**d**), Tarim (**e**) and Inner TP (**f**). Red shadows represent regions showing decreases in TWS, and blue shadows represent regions showing increases in TWS.

The Yellow basin also depends on upstream water supply because the downstream water demand cannot be fully met by NSC_d (Supplementary Table 7). However, future water supply caused by changes in upstream storage may be optimistic because we find an increase in SSC of 7% and in SSCs of 6% relative to the baseline water demand (Fig. 4). Although the future water demand increases by 5%, the total supply capacity (summing NSC_u, NSC_d and SSC) increases by 4%. This indicates that the supply–demand balance may be stable in the Yellow basin in the future.

Discussion

This study investigates climate impacts on past and projected future TWSC over the TP, providing insights into hydrologic processes impacting high-mountain freshwater supplies that serve large
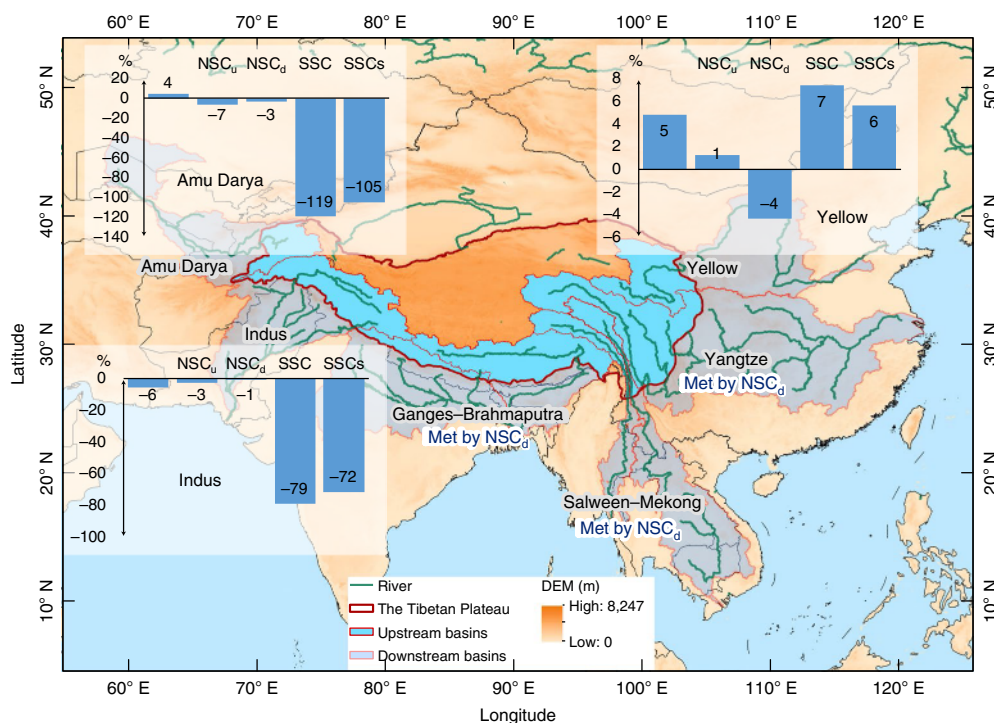
Fig. 4 | Projected changes in water demand and supply capacity in key sian basins. Percentage shows the change between future and present total water demand (*D*), NSC$_u$, NSC$_d$, SSC and SSCs relative to the water-demand baseline. The future period is defined as the mid-twenty-first century (2031–2060), and the present period is defined as the early twenty-first century (2002–2030). The water-demand baseline was estimated as the average total water demand during the 2002–2030 period.

downstream Asian populations. Exorheic TP basins are seen to be most impacted by warming and precipitation decreases related to weakening of the South Asia Summer Monsoon. However, endorheic basins have undergone a wetting climate combined with decreases in surface short-wave radiation since the early twenty-first century. The entire TP is projected to experience a warmer climate by the mid-twenty-first century.

Climate change in recent decades has led to severe depletion in TWS over the entire exorheic basins ($-15.8\,\mathrm{Gt\,yr^{-1}}$) but substantial increases in TWS across the entire endorheic basins ($5.6\,\mathrm{Gt\,yr^{-1}}$). These differential trends reflect the competing effects of glacier retreat, degradation of permafrost and seasonally frozen ground, and lake expansion that are confirmed by multisource remote sensing and land surface model output. These TWSC impact not only water availability (for example, melt water for irrigation), but also natural disaster risk (for example, glacier collapse and glacier lake outburst), threatening compound hydro-political tensions in densely populated downstream areas.

Future TWS projections under the mid-range SSP2–4.5 emissions scenario suggest that the entire TP could experience substantial TWSC with a net loss of ~230 Gt by the mid-twenty-first century (2031–2060) relative to an early twenty-first-century (2002–2030) baseline. Solid-water resources are likely to diminish, particularly over the Amu Darya and Indus basins, where precipitation is projected to be stable while temperature is projected to rise substantially until the mid-twenty-first century. Excess water loss, particularly the severe reduction in solid-water resources, represents a major threat to the stability of two such vulnerable water towers. The decline in upstream supply capacity caused by TWS loss could be up to 119% and 79% of the downstream water-demand baseline in the Amu Darya and Indus basins, respectively. More alternative water-supply sources, including increased groundwater extraction and more water transfer

projects, may be necessary to meet the amplified water shortage in the future.

This study also reveals potential advances in using satellite-based observations and data-driven approaches in hydrologic applications. Combining multisource remote sensing and ensemble mean of LSMs, this study represents an advance relative to previous studies, most of which have neglected evaluation of the constituent contributions to TWSC. In contrast to model-based analysis, data-driven approaches improved inherent limitations in most hydrologic models that exclude water-storage changes in aquifers and largely underestimate TWS trends (see Supplementary Section 3 for further discussion on advantages of machine-learning-based projection).

Despite caveats and uncertainties (Methods) associated, for example, with the extrapolation of relationships established using machine-learning algorithms trained on relatively short datasets, this study identifies hotspots in Asian water towers that are at risk under projected climate change. By examining the interactions between climate change and the terrestrial water system, our study aims to inspire future research and management for governments and institutions towards improved adaptation strategies in coming decades.

Online content

Any methods, additional references, Nature Research reporting summaries, source data, extended data, supplementary information, acknowledgements, peer review information; details of author contributions and competing interests; and statements of data and code availability are available at https://doi.org/10.1038/s41558-022-01443-0.

References

1. Yao, T. et al. The imbalance of the Asian water tower. *Nat. Rev. Earth Environ.* https://doi.org/10.1038/s43017-022-00299-4 (2022).
2. Yao, T. et al. Different glacier status with atmospheric circulations in Tibetan Plateau and surroundings. *Nat. Clim. Change* **2**, 663–667 (2012).
3. Moelg, T., Maussion, F. & Scherer, D. Mid-latitude westerlies as a driver of glacier variability in monsoonal High Asia. *Nat. Clim. Change* **4**, 68–73 (2014).
4. Tapley, B. D. et al. Contributions of GRACE to understanding climate change. *Nat. Clim. Change* **9**, 358–369 (2019).
5. Kraaijenbrink, P. D. A., Bierkens, M. F. P., Lutz, A. F. & Immerzeel, W. W. Impact of a global temperature rise of 1.5 degrees Celsius on Asia's glaciers. *Nature* **549**, 257–260 (2017).
6. Houborg, R., Rodell, M., Li, B., Reichle, R. & Zaitchik, B. F. Drought indicators based on model-assimilated Gravity Recovery and Climate Experiment (GRACE) terrestrial water storage observations. *Water Resour. Res.* **48**, W07525 (2012).
7. Long, D. et al. GRACE satellite monitoring of large depletion in water storage in response to the 2011 drought in Texas. *Geophys. Res. Lett.* **40**, 3395–3401 (2013).
8. Long, D. et al. Drought and flood monitoring for a large karst plateau in Southwest China using extended GRACE data. *Remote Sens. Environ.* **155**, 145–160 (2014).
9. Reager, J. T., Thomas, B. F. & Famiglietti, J. S. River basin flood potential inferred using GRACE gravity observations at several months lead time. *Nat. Geosci.* **7**, 589–593. (2014).
10. Pokhrel, Y. N. et al. Model estimates of sea-level change due to anthropogenic impacts on terrestrial water storage. *Nat. Geosci.* **5**, 389–392 (2012).
11. Jacob, T., Wahr, J., Pfeffer, W. T. & Swenson, S. Recent contributions of glaciers and ice caps to sea level rise. *Nature* **482**, 514–518 (2012).
12. Immerzeel, W. W. et al. Importance and vulnerability of the world's water towers. *Nature* **577**, 364–369 (2020).
13. Scanlon, B. R. et al. Global models underestimate large decadal declining and rising water storage trends relative to GRACE satellite data. *Proc. Natl Acad. Sci. USA* **115**, E1080–E1089 (2018).
14. Pokhrel, Y. N. et al. Incorporation of groundwater pumping in a global land surface model with the representation of human impacts. *Water Resour. Res.* **51**, 78–96 (2015).
15. Pokhrel, Y. et al. Global terrestrial water storage and drought severity under climate change. *Nat. Clim. Change* **11**, 226–233 (2021).
16. Brun, F., Berthier, E., Wagnon, P., Kaab, A. & Treichler, D. A spatially resolved estimate of High Mountain Asia glacier mass balances from 2000 to 2016. *Nat. Geosci.* **10**, 668–673 (2017).
17. Zhao, F., Long, D., Li, X., Huang, Q. & Han, P. Rapid glacier mass loss in the Southeastern Tibetan Plateau since the year 2000 from satellite observations. *Remote Sens. Environ.* **270**, 112853 (2022).
18. Farinotti, D., Immerzeel, W. W., de Kok, R. J., Quincey, D. J. & Dehecq, A. Manifestations and mechanisms of the Karakoram glacier anomaly. *Nat. Geosci.* **13**, 8–16 (2020).
19. Forsythe, N., Fowler, H. J., Li, X.-F., Blenkinsop, S. & Pritchard, D. Karakoram temperature and glacial melt driven by regional atmospheric circulation variability. *Nat. Clim. Change* **7**, 664–670 (2017).
20. Zhang, G. et al. Lake volume and groundwater storage variations in Tibetan Plateau's endorheic basin. *Geophys. Res. Lett.* **44**, 5550–5560 (2017).
21. Li, X. et al. High-temporal-resolution water level and storage change data sets for lakes on the Tibetan Plateau during 2000–2017 using multiple altimetric missions and Landsat-derived lake shoreline positions. *Earth Syst. Sci. Data* **11**, 1603–1627 (2019).
22. Wang, T. et al. Permafrost thawing puts the frozen carbon at risk over the Tibetan Plateau. *Sci. Adv.* **6**, eaaz3513 (2020).
23. Zheng, G. et al. Remote sensing spatiotemporal patterns of frozen soil and the environmental controls over the Tibetan Plateau during 2002–2016. *Remote Sens. Environ.* **247**, 111927 (2020).
24. Rodell, M. et al. Emerging trends in global freshwater availability. *Nature* **557**, 651–659 (2018).
25. Tapley, B. D., Bettadpur, S., Ries, J. C., Thompson, P. F. & Watkins, M. M. GRACE measurements of mass variability in the Earth system. *Science* **305**, 503–505 (2004).
26. Jing, W., Zhang, P. & Zhao, X. A comparison of different GRACE solutions in terrestrial water storage trend estimation over Tibetan Plateau. *Sci. Rep.* **9**, 1765 (2019).
27. Viviroli, D., Kummu, M., Meybeck, M., Kallio, M. & Wada, Y. Increasing dependence of lowland populations on mountain water resources. *Nat. Sustain.* **3**, 917–928 (2020).
28. Zhang, G., Yao, T., Xie, H., Kang, S. & Lei, Y. Increased mass over the Tibetan Plateau: from lakes or glaciers? *Geophys. Res. Lett.* **40**, 2125–2130 (2013).
29. Biemans, H. et al. Importance of snow and glacier meltwater for agriculture on the Indo–Gangetic Plain. *Nat. Sustain.* **2**, 594–601 (2019).
30. Lutz, A. F. et al. South Asian agriculture increasingly dependent on meltwater and groundwater. *Nat. Clim. Change* **12**, 566–573 (2022).
31. Gao, J., Yao, T., Masson-Delmotte, V., Steen-Larsen, H. C. & Wang, W. Collapsing glaciers threaten Asia's water supplies. *Nature* **565**, 19–21 (2019).
32. Liu, B. et al. Causes of the outburst of Zonag Lake in Hoh Xil,Tibetan Plateau, and its impact on surrounding environment. *J. Glaciol. Geocryol.* **38**, 305–311 (2016).
33. Yao, X., Liu, S., Sun, M., Guo, W. & Zhang, X. Changes of Kusai Lake in Hoh Xil region and causes of its water overflowing. *Acta Geogr. Sin.* **67**, 689–698 (2012).
34. Rounce, D. R., Hock, R. & Shean, D. E. Glacier mass change in High Mountain Asia through 2100 using the open-source Python Glacier Evolution Model (PyGEM). *Front. Earth Sci.* **7**, 331 (2020).
35. Qin, Y. et al. Agricultural risks from changing snowmelt. *Nat. Clim. Change* **10**, 459–465 (2020).
36. Jain, M. et al. Groundwater depletion will reduce cropping intensity in India. *Sci. Adv.* **7**, eabd2849 (2021).
37. Murakami, D. & Yamagata, Y. Estimation of gridded population and GDP scenarios with spatially explicit statistical downscaling. *Sustainability* **11**, 2106 (2019).
38. De Stefano, L., Petersen-Perlman, J. D., Sproles, E. A., Eynard, J. & Wolf, A. T. Assessment of transboundary river basins for potential hydro-political tensions. *Glob. Environ. Change* **45**, 35–46 (2017).

Methods

Top-down terrestrial water-storage change. Top-down observations for monthly TWS anomaly (TWSA) during April 2002–June 2017 and June 2018–May 2020 were derived from four GRACE and GRACE-FO solutions[39]: two mascon solutions (JPL-M and CSR-M) based on the latest versions of Release Number 06 (RL06) and two spherical harmonics solutions (JPL-SH and CSR-SH) that are from the versions of RL05. JPL-M and CSR-M data are represented on a nominal resolution of 0.5° and 0.25°, respectively. However, JPL-M represents 3° × 3° equal-area caps of its native resolution whereas CSR-M represents the equal-area geodetic grid of 1° × 1° at the Equator. Two SH products have a nominal resolution of 1° × 1° by applying a 300-km-wide Gaussian filter. However, two neighbouring grid cells of SH products are dependent because of the applied spatial smoothing. All reported GRACE data are anomalies relative to the 2004–2009 time-mean baseline. Missing monthly TWSA during the GRACE period (April 2002–June 2017) caused by instrument failure was linearly interpolated using the nearest two monthly estimates. From the gap period between the GRACE and GRACE-FO missions (July 2017–May 2018), we used machine learning to reconstruct TWSA for each grid cell over the TP. The top-down TWSC can be calculated as the backward difference in TWSA (equation (1)):

$$TWS/ \ t = \frac{TWSA \ t) \quad TWSA \ t \quad 1)}{t} \qquad (1)$$

where t indicates the sequence in monthly TWSA series, and Δt is estimated as one month to be consistent with the temporal resolution of GRACE observations.

To examine long-term trends in TWS variations, we decomposed TWSA time series into the following components[40] (equation (2)):

$$S_{total} = S_{long \ term} + S_{seasonal} + Residuals \qquad (2)$$

where the original signal (S_{total}) was decomposed into long-term variability (including linear trend and interannual variability), seasonal amplitudes and residual components. TWS trend was determined from the slope by applying linear regression to the long-term signal. The non-parametric Seasonal-Trend decomposition procedure based on Loess (STL) approach through a locally weighted regression was used for decomposition[41], which is a robust, a computationally efficient, and the most commonly used approach for detecting nonlinear patterns in GRACE datasets[42,43].

The variance of each temporal component in equation (2) was divided by the variance in the raw time series to estimate relative contributions of each temporal component to the total signal[44]. In addition, the coefficient of determination of the regressed linear trend time series was calculated as a useful piece of evidence to reflect the strength of the linear trends relative to short-term variability[24].

Bottom-up terrestrial water-storage change. TWSC were partitioned into changes in surface (including glacier and lake storages) and subsurface components. Sources of uncertainty in bottom-up TWSC include mainly inconsistencies and different spatial resolutions among various datasets, uncertainty from each component estimation and the neglect of some minor forms of water storage (see Supplementary Section 4 for detailed discussions).

Changes in glacier water storage. The total rate of glacier volume change was calculated as the sum of the mean rate of elevation change multiplied by the area of the glacier mask for each 100-m-elevation band. The rate of volume change was converted to the rate of glacier mass change using a conversion factor (equation (3)):

$$M = \frac{\sum_{i \ 1}^{n} \ h_i \times A_i) \times \rho}{A} \qquad (3)$$

where ΔM is the rate of total glacier mass change; Δh_i is the rate of elevation change for each 100-m-elevation band; A is the glacier area, subscript i represents the area for each 100-m-elevation band; and ρ is the average density of the glacier (or the volume-to-mass conversion factor), which equals $850 \ kg \ m^{-3}$ according to ref. [45].

For rates of elevation change, we used those during the 2000–2016 period provided by Brun et al.[16] that cover 92% of the glacierized area in High Mountain Asia. Here we assumed that changes in glacier water storage during the 2000–2016 period can approximate those during the 2002–2017 period. For a given spatial unit, the elevation-change rate on glaciers was calculated for each 100-m-elevation band as the mean of all pixels belonging to this band. If no data were available for an elevation band (for example, the uppermost reaches), a zero value was assigned to the elevation-change rate. The glacier mask was determined by the latest Randolph Glacier Inventory (RGI 6.0).

Changes in lake water storage. Changes in lake water storage over the TP except the Inner TP and Qaidam basins were provided by Li et al.[21]. Combining multiple altimetric missions and optical remote-sensing images, the resulting high-temporal resolution (monthly) datasets help resolve interannual and intra-annual variability and trends in lake water storage. Storage variations for 52 large lakes (≥100 km²; accounting for ~60% of the total TP lake area) during the 2000–2017 period are

available at weekly to monthly timescales. The estimated uncertainty in the water level is ~0.1 m on the basis of rigorous examination of both field experiments and theoretical verification. Uncertainty in lake storage trends is ~6% for the entire TP through uncertainty propagation. The Inner TP and Qaidam basins contain a large number of small lakes; therefore, we used the latest dataset from Wang et al.[46], which covers 930 lakes in the Inner TP basin and 46 lakes in the Qaidam basin (≥1 km²). This dataset is based on Landsat-derived annual lake area changes and digital elevation model (DEM)-derived lake elevation–area relationships (hypsometric curves). Despite discrepancy in relatively small lakes, lake storage changes from Wang et al.[46] are overall consistent with those from Li et al.[21] in 40 overlapping lakes; that is, 26 overlapping lakes between the two datasets have correlation coefficients higher than 0.8.

Changes in subsurface water storage. To estimate changes in subsurface water storage, we incorporated the latest estimates from three LSMs: NOAH -3.6 (0.25° × 0.25°) and VIC-4.1.2 (1° × 1°) from Global Land Data Assimilation System 2.1 (GLDAS-2.1) and CLSM-F2.5 (0.25° × 0.25°) from GLDAS-2.2. Here we summed storage for each depth interval to represent total subsurface water storage (four layers of soil water for NOAH, three layers of soil water for VIC, and root zone soil water and groundwater for CLSM). Differences in modelled subsurface depths were not considered. For each model, subsurface water-storage anomalies were calculated by subtracting the 2004–2009 time-mean baseline to be consistent with GRACE data. In addition, subsurface water-storage anomalies were decomposed using the STL approach[41], and the storage trend was determined by applying linear regression to the decomposed long-term variability. Finally, we calculated the mean trends of three LSMs for each basin. Note that CLSM generates outputs since 2003, and thus we assumed that CLSM-based changes in subsurface storage during the 2003–2017 period can approximate those during the 2002–2017 period.

Reconstruction and projection of TWSA using machine learning. We used machine-learning-based artificial neural network (ANN) models to train and predict TWSA for each grid cell (0.5°) on the TP during the gap period between the GRACE and GRACE-FO missions (July 2017–May 2018) and up to the mid-twenty-first century until 2060. Machine learning was selected over hydrologic models because (1) the latter do not include some of the aquifers and greatly underestimate the linear trends in TWSA[13,47] (see Supplementary Section 3 for detailed discussion) and (2) machine-learning approaches can efficiently model nonlinear relationships between inputs and outputs[48]. Machine learning has been successfully applied to reconstruct GRACE data (or more precisely, GRACE-like data)[47,49,50]. However, we acknowledge that TWSA reconstruction over the high-mountain TP is challenging due to the complex relationship between climate forcing and water storage. Most previous machine-learning studies relied on monthly precipitation, temperature and modelled soil water storage for reconstructing GRACE-like TWSA, which could have good performance in humid regions but poor results over glacierized areas in the TP[50] (see Supporting Section 3).

To explore the potential of machine-learning approaches in reconstructing and projecting TWSA over the TP, we improved the input layer on the basis of the water balance principle (input fluxes – output fluxes = TWS changes). Although machine learning does not explicitly show physical processes, hydrologic principles could be used in the input layer to improve its performance. TWS can be calculated using equation (4):

$$\begin{aligned}
TWS_n &= TWS_0 + \ TWS_1 + \ TWS_2 + \cdots + \ TWS_n \\
&= TWS_0 + \ flux_{In,1} \quad flux_{Out,1}) + \ flux_{In,2} \quad flux_{Out,2}) \\
&\quad + \cdots + \ flux_{In,n} \quad flux_{Out,n}) \\
&= TWS_0 + \ flux_{In,1} + flux_{In,2} + \cdots + flux_{In,n}) \\
&\qquad flux_{Out,1} + flux_{Out,2} + \cdots + flux_{Out,n})
\end{aligned} \qquad (4)$$

Equation (4) implies that the state variable (TWS) is affected by accumulated flux variables in a given period. Thus, combining accumulated flux variables and related state variables could be one reasonable way for predicting target TWS using machine learning. Here the target variable was GRACE-derived TWSA estimated from JPL-M due to its good agreement with bottom-up TWSA as illustrated in the preceding. The forcing data (predictors) of the input layer included bias-corrected precipitation, air temperature and surface short-wave radiation derived from nine CMIP6 models and simulated TWS from the latest CMIP6 CESM2–WACCM model. Flux variables (precipitation and surface short-wave radiation) were accumulated for the previous period ahead of the projected time, whereas state variables (air temperature and modelled TWS) were directly input. All input variables were divided into the historical (2002–2020) and future (2021–2060) periods for bias correction. They were normalized by subtracting the 2004–2009 time-mean baseline to be consistent with the target variable (GRACE TWSA).

The risk of overfitting using overly complex machine-learning models requires caution because the number of target data is relatively small (GRACE and GRACE-FO observations of 207 months in total; April 2002–May 2020

except the gap period of July 2017–May 2018). Therefore, we chose the basic machine-learning structure (ANN) and strictly set only one or two hidden layers with four neurons for each layer. The small number of hidden layers and neurons could effectively reduce the risk of overfitting from the model structure. In addition, the ANN models were trained at the 0.5° grid-cell scale (rather than the basin scale) over the TP, indicating that we built 1,191 different ANN models over the TP. For each grid cell, the forcing and target data during the periods with GRACE or GRACE-FO observations (207 months in total) were randomly divided into training, validation and testing sets, accounting for ~70%, 15% and 15% of the samples, respectively. The reconstructed TWSA at the 0.5° grid cell was spatially filtered using the disk-filtering method with a radius of three. This was to exclude outliers, and the filtering radius considered the difference between the native (3°×3° equal-area caps) and nominal (0.5°×0.5°) resolution of GRACE JPL-M. As for TWSA projection, we assumed that the determined nonlinear relationship between the input layer and target TWSA in the past could be transferable to the future. Uncertainty in TWSA projection was estimated as ±1 standard deviation among outputs from different CMIP6 forcings.

The activation functions were 'tansig', 'logsig' and 'purelin', which are the most commonly used functions in the hydrologic field[50]. Model frameworks, activation/transfer functions and optimization methods were tested to determine optimal parameters on the basis of the Kling–Gupta efficiency (KGE)[51,52] (equation (5)) between observed and modelled TWSA values of the testing samples.

$$KGE = 1 - \sqrt{(r-1)^2 + (\beta-1)^2 + (\gamma-1)^2}$$ (5)

where r is the correlation coefficient that reflects the consistency in timing, β is the bias ratio of the mean of the modelled values to the mean of the observations and γ is the variability ratio of the standard deviation of the modelled values to the standard deviation of the observations. KGE is a comprehensive indicator of performance that includes correlation, ratio of means and ratio of dispersion of the two paired datasets, with a perfect fit indicated by a value of 1 on all metrics.

Corrections of forcing data derived from climate models. Climate forcings for the ANN models, including precipitation, temperature and surface short-wave radiation, were derived from nine climate models that have relatively high spatial resolution (a nominal resolution of $100\,km \times 100\,km$) from the CMIP6 database (Supplementary Table 3). In addition, ET was derived from nine models to quantify water-supply capacity. These data were obtained at the daily timescale from CMIP6 ScenarioMIP covering both historical (1980–2014) and future (2015–2100) periods under the moderate forcing scenario (SSP2–4.5). Considering large systematic errors in climate models due to the simplified physical processes and numerical schemes[53], bias correction is required for all datasets. Here global outputs from CMIP6 climate models were resampled to 0.5°×0.5° grid cells for matching the nominal resolution of JPL-M datasets on the basis of the bilinear method. For each variable, daily estimates were used in bias correction, and then the corrected data were averaged or aggregated to monthly timescales. The baseline and prediction periods for correcting climate model outputs were set as 2002–2020 and 2021–2060, respectively.

The delta approach was used to bias correct air temperature, surface short-wave radiation and ET estimates in both baseline and prediction periods[54], as given by equation (6).

$$T_c = T_m - (\overline{T_{m,b}} - \overline{T_{ref,b}})$$ (6)

where T means the daily air temperature; subscripts c and m represent the corrected data and modelled data derived from climate models, respectively; subscript b refers to the baseline period (2002–2020); subscript ref represents the reference data for bias correction, which is air temperature estimated from ERA5 reanalysis datasets[55] in this study; and an overbar denotes the mean. Equation (6) could also be applied to surface short-wave radiation and ET correction. The baseline radiation datasets can be derived from ERA5 reanalysis, and baseline ET datasets can be derived from the Global Land Evaporation Amsterdam Model v.3.5a (GLEAM v.3.5a) due to its good performance over the TP[56].

A more sophisticated approach, quantile mapping (QM), was used for bias correction for precipitation[57]. This is because climate model outputs are known to have a drizzle problem that shows many low-magnitude rain events compared with observations[58]. In addition, climate models have difficulty in capturing realistic interannual variability. The QM method includes calculation of cumulative distribution functions (CDFs) for observed and modelled data during the baseline period (equation (7)) and then uses a transfer function (equation (8)) for bias correction.

$$P_o = h[P_m]$$ (7)

$$P_c = F_o^{-1}\{F_m[P_m]\}$$ (8)

where P refers to the daily precipitation; subscripts o, m and c represent the observed, modelled and corrected precipitation, respectively; h is the function that maps the modelled data to the same distribution as the observed data; F refers to the CDF function; and F^{-1} refers to the inverse CDF function. Here precipitation

from the Integrated Multi-satellite Retrievals for GPM (IMERG) V06[59] was regarded as the observed data, and we used the empirical CDF of the observed and modelled time series for regularly spaced quantiles. Due to significant seasonality over the TP, we implemented the QM bias correction for precipitation month by month, for example, as for bias correction for precipitation in January, all daily precipitation in January during 2002–2020 and 2021–2060 was used to calculate cumulative distribution functions for baseline and prediction periods, respectively.

Quantifying water demand and supply capacity. Conceptually, a high-mountain water tower is deemed to be important when its water resources (liquid or frozen) are plentiful relative to its downstream water demand and when its basin water demand is high and cannot be met by downstream water availability alone[12]. Here we considered human water demand for irrigation, industrial and domestic purposes[60], all of which were estimated under a mid-range scenario (SSP2 and representative concentration pathway 6.0). Irrigation water demand was estimated from actual irrigation withdrawal from a widely used global vegetation model (Lund–Potsdam–Jena-managed land model) provided by the Inter-Sectoral Impact Model Intercomparison Project portal. Industrial and domestic water demand was provided from the International Institute for Applied Systems Analysis. These datasets were widely used in examining supply–demand relationships[12,29]. Here we considered only downstream water demand because (1) the population and water use over the high-mountain TP are pretty low and (2) this study focuses on the supply linkage between upstream water towers and downstream areas.

We considered three supply sources for downstream water availability: NSC_u, NSC_d and SSC from upstream basins. Although other water sources, for example, groundwater in downstream areas, can also be important, we focused more on the impacts from upstream TWS changes and considered other sources as the alternative water supply, similar to what Immerzeel et al.[12] and Qin et al.[35] conducted. NSC was defined as precipitation minus actual ET[12], indicating water supply from the difference between water input and output fluxes. Both precipitation and ET were derived from the ensemble mean of nine climate models and corrected on the basis of IMERG and GLEAM products, respectively. SSC was defined as TWS, the maximum water amount that can be used by downstream areas. We assumed that the contribution of changes in surface storage to TWS changes remains the same in the future as that during the GRACE period. Thus, we could further quantify SSCs, which could be directly used by downstream areas.

Because GRACE estimated TWSA (anomalies relative to the mean of 2004–2009) rather than the absolute TWS, here we focused on changes in NSC and SSC in the future relative to the water-demand baseline. Taking average total water demand during the early twenty-first century (2002–2030) as the baseline, this study calculated the percentage of changes in mean annual supply capacity during the mid-twenty-first century (2031–2060) relative to that during the early twenty-first century (2002–2030) to the demand baseline. For example, the relative change in SSC was calculated as: $(\overline{SSC_{2031-2060}} - \overline{SSC_{2002-2030}})/\overline{D_{2002-2030}}$.

Caveats and uncertainties. Among the caveats and uncertainties in our analysis is the combination of different data sources, which makes formal uncertainty estimation challenging. Inconsistencies among datasets and the neglect of some forms of water storage also result in uncertainty in the bottom-up estimates of TWS changes (Supplementary Section 4). The spatial resolution of GRACE datasets is relatively coarse, resulting in added uncertainty in basin-averaged TWS trends. In addition, although precipitation, temperature and surface short-wave radiation are three critical climate drivers, additional mechanisms (such as ET[61], morphology[62] and the glacier state of debris cover[18]) should be considered in local studies. Finally, despite the skilful performance of the machine-learning approach in capturing complex relationships among different variables, there is uncertainty using such relationships for future projections owing to the potential limitations in statistical stationarity assumptions.

Data availability
Shapefiles of hydrologic basin boundaries[63] used in this study are provided at http://data.tpdc.ac.cn. GRACE and GRACE-FO data are provided by the NASA MEaSUREs Program, where SH and JPL-M data can be accessed at https://grace.jpl.nasa.gov/; and the CSR-M data can be accessed at http://www2.csr.utexas.edu/grace. The elevation-change maps over the glacierized areas[64] are provided at https://doi.org/10.1594/PANGAEA.876545, and RGI 6.0 glacier mask can be accessed at http://www.glims.org/RGI/. Datasets of lake storage changes[46,65] are available at https://doi.org/10.5281/zenodo.5543615 and https://doi.org/10.1594/PANGAEA.898411. Data from GLDAS land surface models and IMERG precipitation can be accessed at https://disc.gsfc.nasa.gov/. ERA5 reanalysis data are available at https://cds.climate.copernicus.eu/. GLEAM ET data are available at https://www.gleam.eu/. Data from CMIP6 models can be found at https://esgf-node.llnl.gov/. Irrigation water demand is derived from the LPJml model provided by the ISIMIP portal (https://www.isimip.org/outputdata/). Industrial and domestic water demand is available on request from Y. Wada (wada@iiasa.ac.at). Monsoon monitor results for generating Supplementary Fig. 8 are derived at http://apdrc.soest.hawaii.edu/projects/monsoon/. Model-simulated TWS for generating Supplementary Fig. 10 is available at https://www.isimip.org/outputdata/. Reservoir information for generating Supplementary Fig. 18 can be

accessed at https://globaldamwatch.org. Data for generating Supplementary Figs. 1, 6 and 11 are accessible on request from Y. Pokhrel (ypokhrel@egr.msu.edu), G. Zheng (zhengguanheng163@163.com) and Z. Sun (sunzhangli@gmail.com), respectively. Projected TWS changes by the mid-twenty-first century, generated by this study[66], are available at https://doi.org/10.5281/zenodo.6784501.

Code availability

References

39. Landerer, F. W. et al. Extending the global mass change data record: GRACE follow-on instrument and science data performance. *Geophys. Res. Lett.* **47**, e2020GL088306 (2020).
40. Scanlon, B. R. et al. Global evaluation of new GRACE mascon products for hydrologic applications. *Water Resour. Res.* **52**, 9412–9429 (2016).
41. Cleveland, R. B., Cleveland, W. S., McRae, J. E. & Terpenning, I. STL: a seasonal-trend decomposition procedure based on loess. *J. Off. Stat.* **6**, 3–73 (1990).
42. Bergmann, I., Ramillien, G. & Frappart, F. Climate-driven interannual ice mass evolution in Greenland. *Glob. Planet. Change* **82-83**, 1–11 (2012).
43. Frappart, F., Ramillien, G. & Ronchail, J. Changes in terrestrial water storage versus rainfall and discharges in the Amazon basin. *Int. J. Climatol.* **33**, 3029–3046 (2013).
44. Rateb, A. et al. Comparison of groundwater storage changes from GRACE satellites with monitoring and modeling of major US aquifers. *Water Resour. Res.* **56**, e2020WR027556 (2020).
45. Huss, M. Density assumptions for converting geodetic glacier volume change to mass change. *Cryosphere* **7**, 877–887 (2013).
46. Wang, J., Wang, L., Li, M., Zhu, L. & Li, X. Lake area and volume variation data in the endorheic basin of the Tibetan Plateau from 1989 to 2019. *Zenodo* https://doi.org/10.5281/zenodo.5543615 (2021).
47. Sun, A. Y. et al. Combining physically based modeling and deep learning for fusing GRACE satellite data: can we learn from mismatch? *Water Resour. Res.* **55**, 1179–1195 (2019).
48. Govindaraju, R. S. & Artific, A. T. C. A. Artificial neural networks in hydrology. I: preliminary concepts. *J. Hydrol. Eng.* **5**, 115–123 (2000).
49. Sun, A. Y., Scanlon, B. R, Save, H. & Rateb, A. Reconstruction of GRACE total water storage through automated machine learning. *Water Resour. Res.* **57**, e2020WR028666 (2020).
50. Sun, Z., Long, D., Yang, W., Li, X. & Pan, Y. Reconstruction of GRACE data on changes in total water storage over the global land surface and 60 basins. *Water Resour. Res.* **56**, e2019WR026250 (2020).
51. Gupta, H. V., Kling, H., Yilmaz, K. K. & Martinez, G. F. Decomposition of the mean squared error and NSE performance criteria: implications for improving hydrological modelling. *J. Hydrol.* **377**, 80–91 (2009).
52. Kling, H., Fuchs, M. & Paulin, M. Runoff conditions in the upper Danube basin under an ensemble of climate change scenarios. *J. Hydrol.* **424**, 264–277 (2012).
53. Ramirez-Villegas, J., Challinor, A. J., Thornton, P. K. & Jarvis, A. Implications of regional improvement in global climate models for agricultural impact research. *Environ. Res. Lett.* **8**, 024018 (2013).
54. Hawkins, E., Osborne, T. M., Ho, C. K. & Challinor, A. J. Calibration and bias correction of climate projections for crop modelling: an idealised case study over Europe. *Agric. For. Meteorol.* **170**, 19–31 (2013).
55. Hersbach, H. et al. The ERA5 global reanalysis. *Q. J. R. Meteorol. Soc.* **146**, 1999–2049 (2020).
56. Li, X. et al. Evapotranspiration estimation for Tibetan Plateau headwaters using conjoint terrestrial and atmospheric water balances and multisource remote sensing. *Water Resour. Res.* **55**, 8608–8630 (2019).
57. Cannon, A. J., Sobie, S. R. & Murdock, T. Q. Bias correction of GCM precipitation by quantile mapping: how well do methods preserve changes in quantiles and extremes? *J. Clim.* **28**, 6938–6959 (2015).
58. Gutowski, W. J. et al. Temporal–spatial scales of observed and simulated precipitation in central US climate. *J. Clim.* **16**, 3841–3847 (2003).
59. Tan, J., Huffman, G. J., Bolvin, D. T. & Nelkin, E. J. IMERG V06: changes to the morphing algorithm. *J. Atmos. Ocean. Technol.* **36**, 2471–2482 (2019).
60. Wada, Y., de Graaf, I. E. M. & van Beek, L. P. H. High-resolution modeling of human and climate impacts on global water resources. *J. Adv. Model. Earth Syst.* **8**, 735–763 (2016).
61. Wang, J. et al. Recent global decline in endorheic basin water storages. *Nat. Geosci.* **11**, 926–932 (2018).
62. Hewitt, K. Glacier change, concentration, and elevation effects in the Karakoram Himalaya, Upper Indus Basin. *Mt. Res. Dev.* **31**, 188–200 (2011).
63. Zhang, J. *Dataset of River Basins map over the TP (2016)* (National Tibetan Plateau Data Center, 2019); https://doi.org/10.11888/BaseGeography.tpe.249465.file
64. Brun, F., Berthier, E., Wagnon, P., Kääb, A. & Treichler, D. Elevation changes of High Mountain Asia from 2000 to 2016, links to GeoTIFFs. *PANGAEA* https://doi.org/10.1594/PANGAEA.876545 (2017).
65. Li, X. et al. A high temporal resolution lake data set from multisource altimetric missions and Landsat archives of water level and storage changes on the Tibetan Plateau during 2000–2017. *PANGAEA* https://doi.org/10.1594/PANGAEA.898411 (2019).
66. Li, X. Y. et al. Supplementary data to: Climate change threatens terrestrial water storage over the Tibetan Plateau. *Zenodo* https://doi.org/10.5281/zenodo.6784501 (2022).
67. Li, X. Y. & Long, D. Supplementary code to: Climate change threatens terrestrial water storage over the Tibetan Plateau. *Zenodo* https://doi.org/10.5281/zenodo.6784641 (2022).

uthor contributions

D.L. and Xueying Li developed the methodology of this study. Xueying Li and D.L. performed the analysis with additional support from B.R.S., M.E.M., Xingdong Li, F.T., Z.S. and G.W. All authors discussed the results and improved the writing of this manuscript.

Competing interests

The authors declare no competing interests.
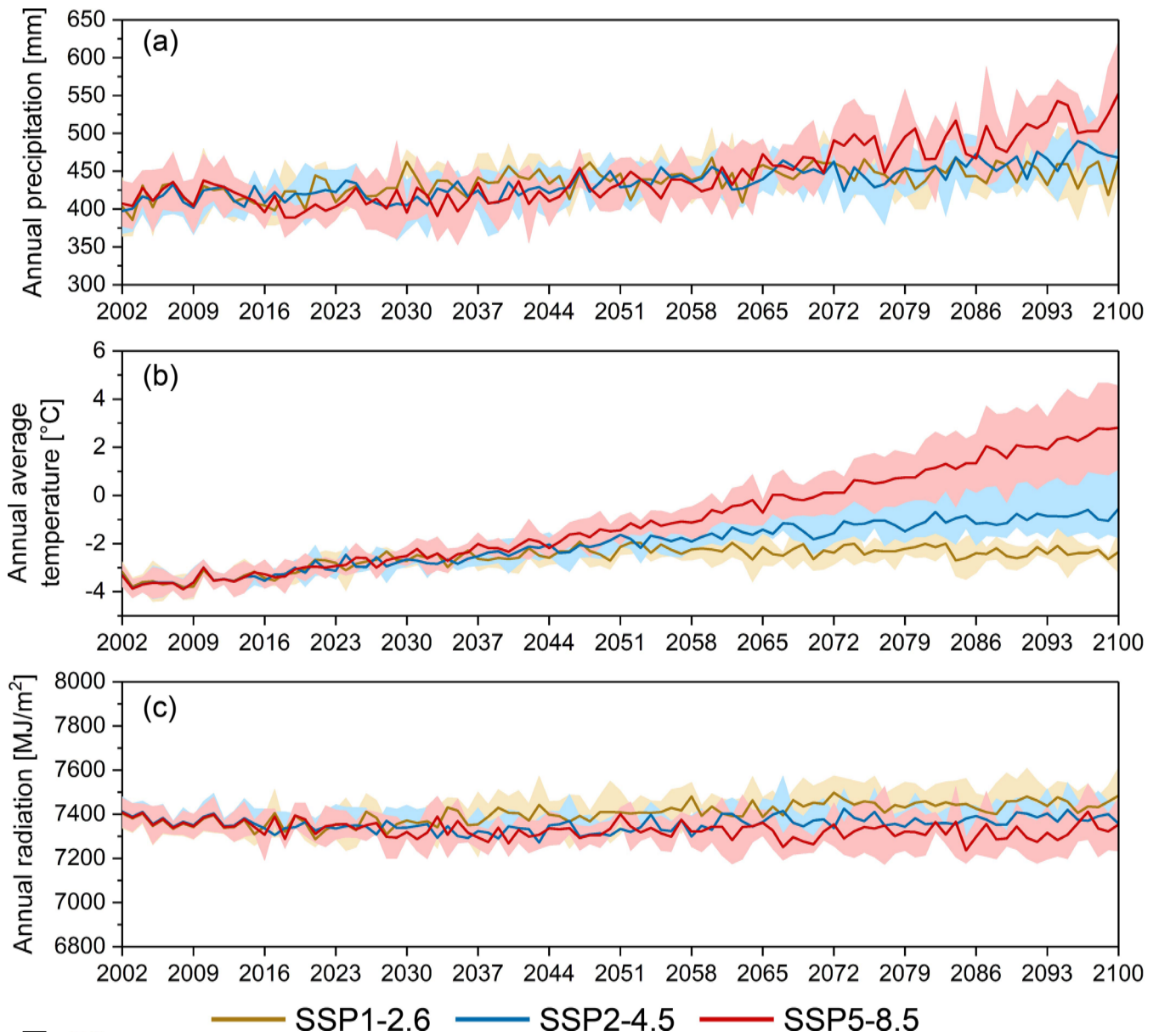
Extended Data Fig. 1 | Projected changes in climate variables over the Tibetan Plateau up to 2100. (**a**) annual average temperature, (**b**) annual precipitation, and (**c**) annual surface short-wave radiation for the 2002–2100 period were estimated by the ensemble mean of nine CMIP6 models under SSP1-2.6, SSP2-4.5, and SSP5-8.5 scenarios. Both temperature and surface short-wave radiation were bias corrected using the delta approach, and precipitation was corrected using the quantile mapping approach. Shadows represent uncertainty range of ±1 standard deviation among outputs from different models.
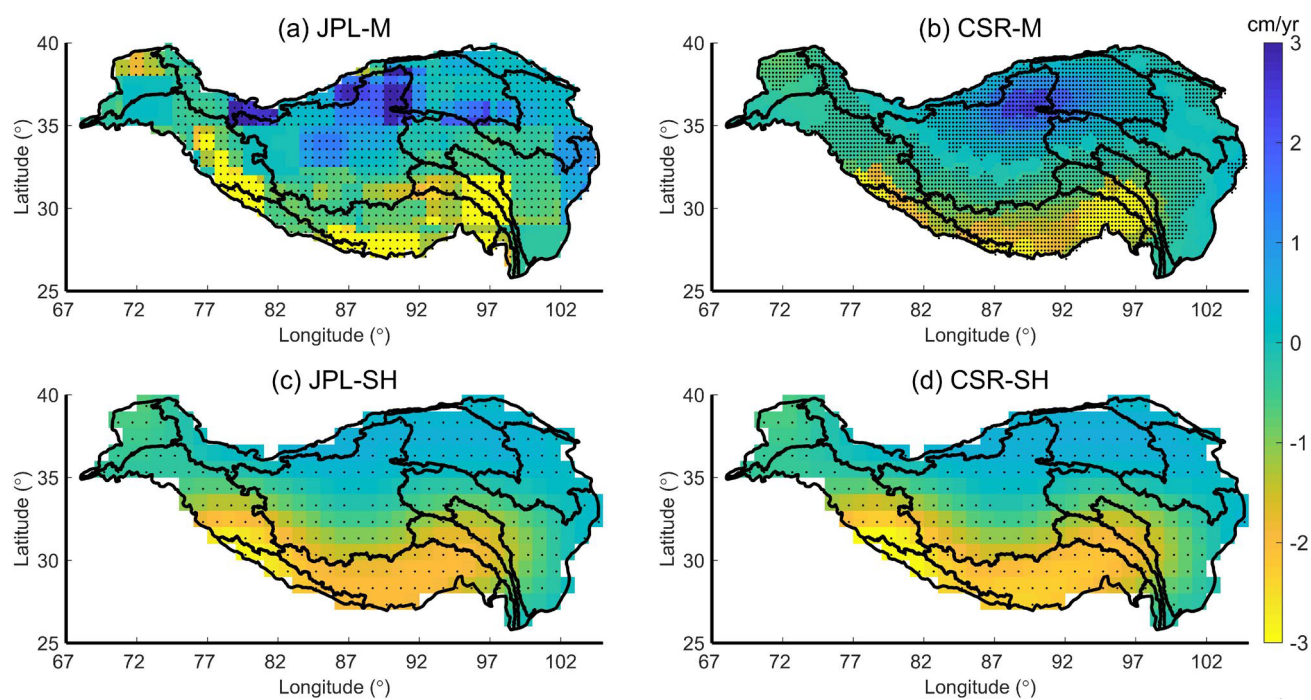
Extended Data Fig. 2 | Trends in terrestrial water storage over the Tibetan Plateau during 2002–2017. Results were derived from four GR CE solutions, that is, (**a**) JPL-M, (**b**) CSR-M, (**c**) JPL-SH, and (**d**) CSR-SH. Stippling marks regions that have a significant trend (the Mann-Kendall test at a 5% significance level).
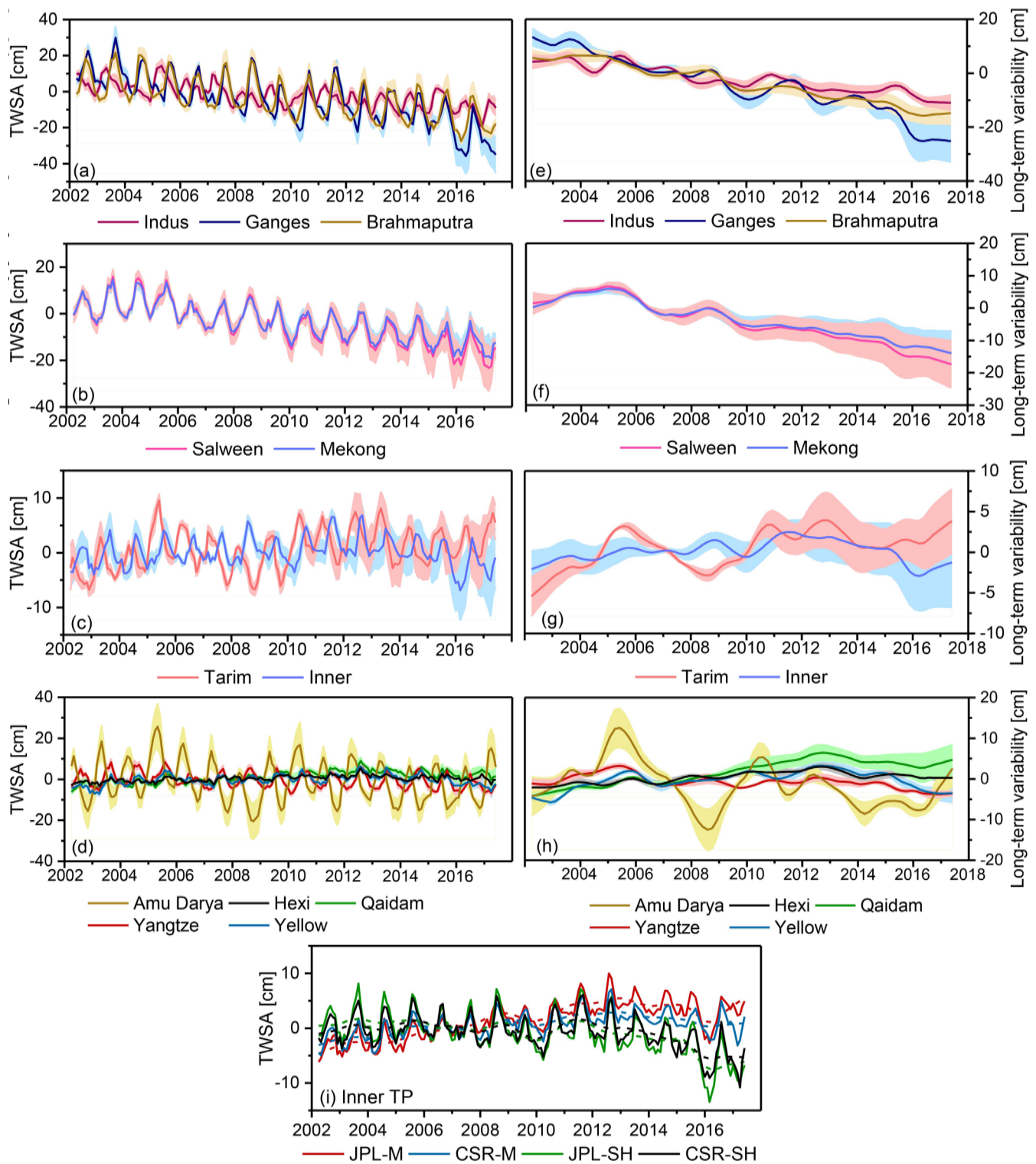
Extended Data Fig. 3 | Terrestrial water storage anomalies and decomposed long-term variabilities. Monthly time series of (**a**–**d**) terrestrial water storage anomaly (TWS) and (**e**–**h**) long-term variability are shown in twelve basins during pr 2002–Jun 2017. Solid lines are the mean of four GR CE solutions (JPL-M, CSR-M, JPL-SH, and CSR-SH), and shadows represent ±1 standard deviation among different solutions. In particular, TWS derived from different GR CE solutions in the Inner TP is shown in (**i**) as an example, where TWS is shown in solid lines and long-term variability is shown in dash lines.
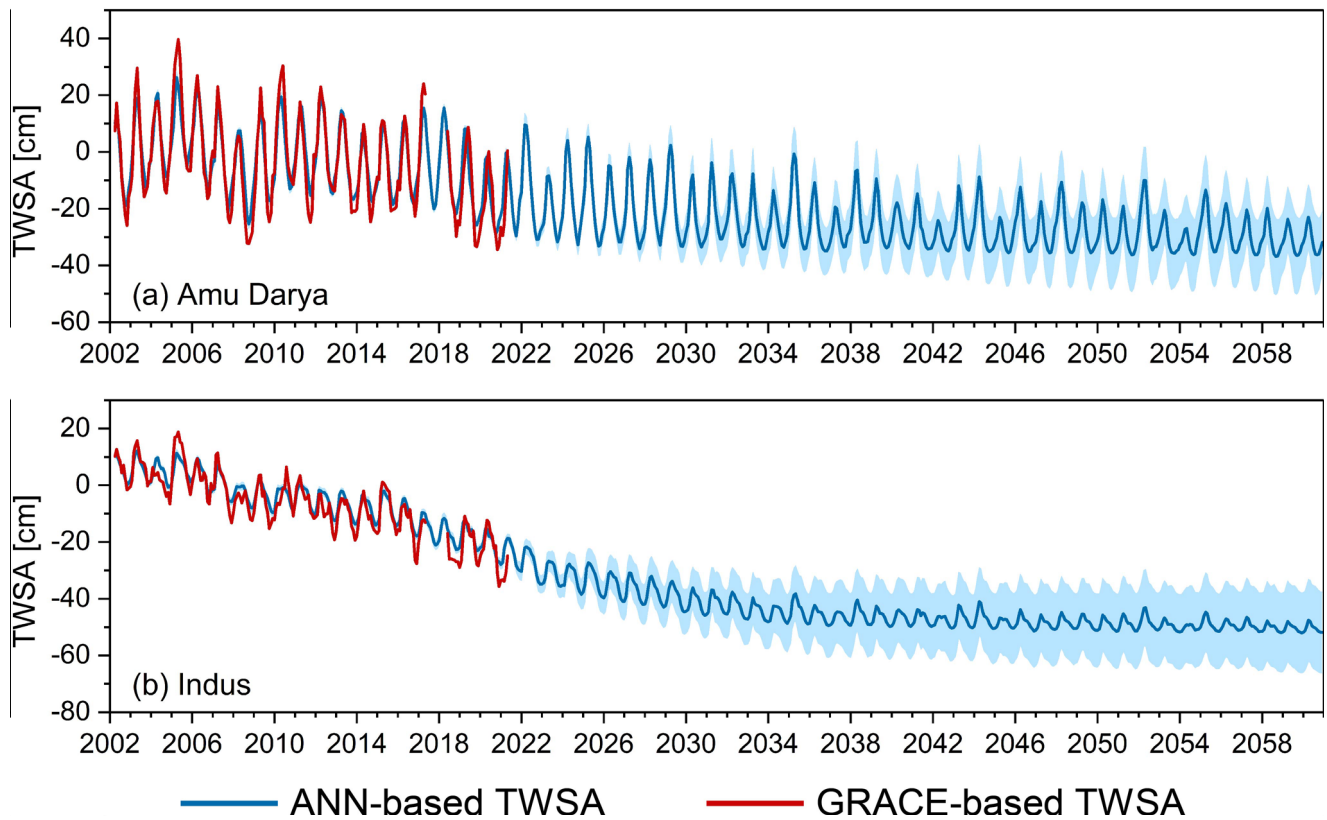
Extended Data Fig. 4 | Observed and projected terrestrial water storage anomalies. Red lines show GR CE observations from JPL-M during 2002–2017, whereas blue lines show the ensemble mean of machine-learning outputs from nine CMIP6 forcings during 2002–2060 in the (**a**) mu Darya and (**b**) Indus basins. Shadows represent uncertainty range of ±1 standard deviation among outputs from different CMIP6 forcings.
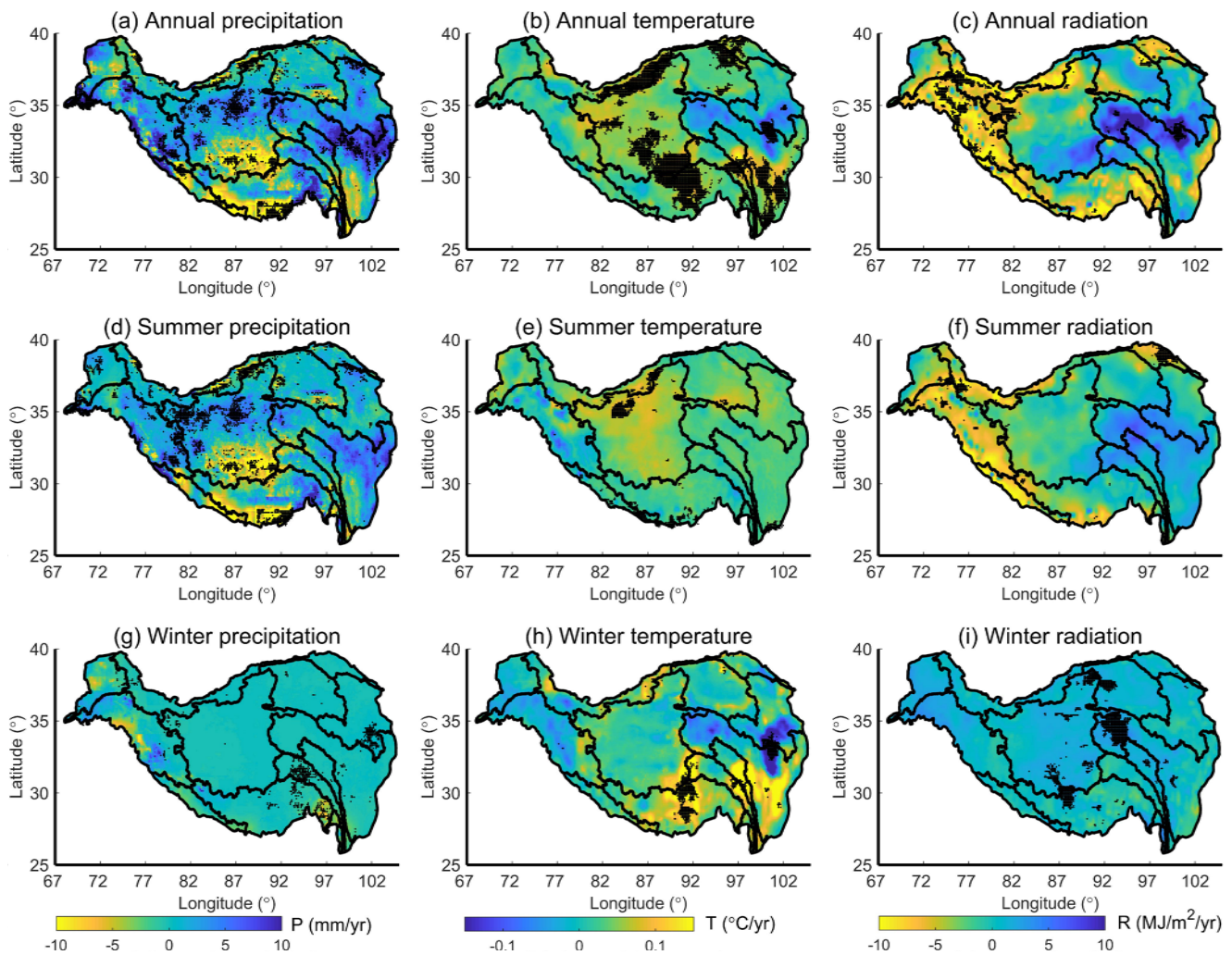
Extended Data Fig. 5 | Trends in climate drivers over the Tibetan Plateau during 2002–2017. Precipitation, temperature, and surface short-wave radiation are analyzed during (**a**–**c**) annual, (**d**–**f**) summer (June– ugust), and (**g**–**i**) winter (December–February) periods. Stippling marks regions that have a significant trend (the Mann-Kendall test at a 5% significance level). Precipitation data were derived from Integrated Multi-satellitE Retrievals for GPM (IMERG) V06, and temperature and radiation data were derived from reanalysis ER 5 data.